

Exciton vortices in two-dimensional hybrid perovskite monolayers

Yingda Chen,^{1,2} Dong Zhang,^{1,2,*} and Kai Chang^{1,2,3,†}

¹SKLSM, Institute of Semiconductors, Chinese Academy of Sciences, P.O. Box 912, Beijing 100083, China

²CAS Center for Excellence in Topological Quantum Computation, University of Chinese Academy of Sciences, Beijing 100190, China

³Beijing Academy of Quantum Information Sciences, Beijing 100193, China

We study theoretically the exciton Bose-Einstein condensation and exciton vortices in a two-dimensional (2D) perovskite (PEA)₂PbI₄ monolayer. Combining the first-principles calculations and the Keldysh model, the exciton binding energy of (PEA)₂PbI₄ in a monolayer can approach hundreds meV, which make it possible to observe the excitonic effect at room temperature. Due to the large exciton binding energy, and hence the high density of excitons, we find that the critical temperature of the exciton condensation could approach the liquid nitrogen regime. In presence of perpendicular electric fields, the dipole-dipole interaction between excitons is found to drive the condensed excitons into patterned vortices, as the evolution time of vortex patterns is comparable to the exciton lifetime.

PACS numbers:

Excitons, the composed bosons formed by bound electron-hole pairs through Coulomb interactions, may collapse into Bose-Einstein condensation (BEC) states at low temperatures¹⁻³. Bosons at the BEC regime not only show exotic superfluidity⁴, but also possess patterns of vortices^{5,6}. Such phenomena have been studied both theoretically and experimentally recently in solids^{7,8}, such as two-dimensional transitional metal dichalcogenides⁹. To realize the exciton BEC, one need to find a system with long exciton lifetime, huge binding energy and small exciton mass. Long exciton radiative lifetime allows the excitons to build up a quasi-equilibrium before recombination, while the huge binding energy leads to small Bohr radius of excitons with high average exciton density. The 2D perovskite monolayers could offer us a possible platform, promising considerably high critical temperature of the exciton BEC.

In the past decades, hybrid organic-inorganic lead halide perovskites have achieved remarkable records in the field of solar cells¹⁰⁻¹³, and shown immense potentials as low-cost alternatives to traditional semiconductors in commercial photovoltaic industry^{14,15}. Comparing to the three-dimensional (3D) perovskites, 2D layered hybrid perovskites possess superior environment stability in device performances^{16,17}, and provide versatile blocks in dimensionality engineering^{18,19} of multi-dimensional perovskites due to the structural diversity^{20,21}. Surprisingly, the 2D hybrid perovskites display huge exciton binding energies about hundreds meV²²⁻²⁴ and long exciton lifetimes about 2.5 ns²⁵, even in presence of high defects and disorders, due to the quantum confinement effects. The two distinguished features make 2D hybrid organic-inorganic lead halide perovskites monolayers as ideal platforms to realize exciton BEC.

In this work, we focus on the typical 2D hybrid perovskite (PEA)₂PbI₄^{23,26-28}. The (PEA)₂PbI₄ possesses a stable layered structure, which comprises alternatively stacked layers of [PbI₆]⁴⁻ octahedra and long-chain organic molecules C₆H₅C₂H₄NH₃⁺ (PEA⁺) as shown in Fig. 1(a). To determine both the crystalline structures and electronic structures, the first-principles calculations are performed by using the Vienna ab initio simulation package (VASP) within the generalized

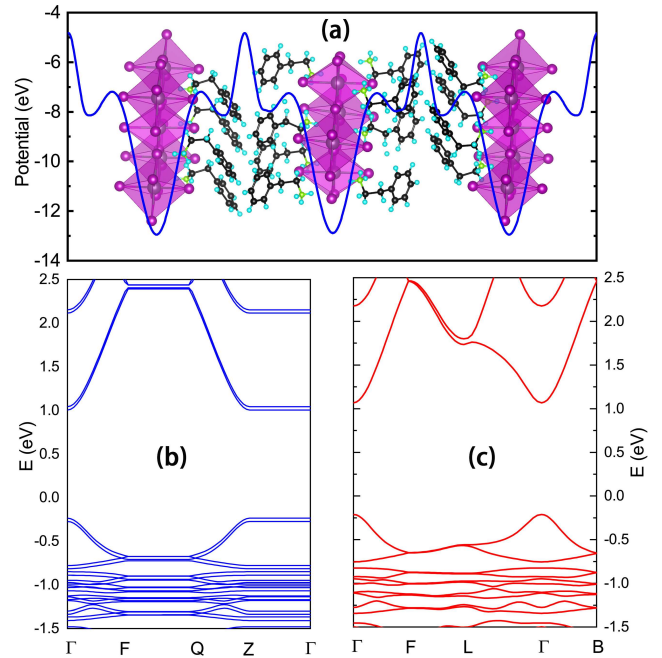


FIG. 1: (a) Schematic of layered hybrid perovskite (PEA)₂PbI₄, for simplicity, the inequivalent two layers are labelled as Layer A and Layer B. The different atoms are indicated by different colour coding, and the effective inner potential is shown by blue solid lines. The lead, iodide, carbon, hydrogen and nitrogen atoms are displayed by silver, purple, black, cyan and green spheres, respectively. (b) Band structures of bulk (PEA)₂PbI₄. (c) Band structures of (PEA)₂PbI₄ monolayer.

gradient approximation (GGA) in Perdew-Burke-Ernzerhof (PBE) type and the projector augmented-wave (PAW) pseudopotential. The kinetic energy cutoff is set to 500 eV for wave-function expansion, and the Monkhorst-Pack type k-point grid is sampled by sums over $3 \times 3 \times 3$. For the convergence of the electronic self-consistent calculations, the total energy difference criterion is set to 10^{-8} eV. The crystal structure is fully relaxed until the residual forces on atoms are less

than 0.01 eV/Å. The spin-orbital coupling effect is taken into consideration, and the van der Waals correction is also included by DFT-D2 method.

From Fig. 1(a), one can see that the inorganic layers PbI_4 are sandwiched between two organic layers, with the effective potential barriers as high as 8.1 eV, as illustrated by the blue solid curves. Such high potential barriers make $(\text{PEA})_2\text{PbI}_4$ behaves like stacking quantum wells with hard-wall confining potentials. Due to the weak interlayer Van der Waals coupling, we find the electronic structures are similar between the bulk material and its monolayer. The band structures are shown in Fig 1(c) all over high symmetric reciprocal points indicated in the Brillouin zone. The parabolic conduction and valence bands are isolated with bulk bands, and possess a direct band gap estimated as 1.24 eV. The direct band gap feature ensures good performance of $(\text{PEA})_2\text{PbI}_4$ in optoelectronic devices. Notice that the band structures of the $(\text{PEA})_2\text{PbI}_4$ monolayer (See Fig. 1(c)) possess a direct band gap about 1.278 eV at the Γ point. Unlike other 2D materials whose band gap vary significantly as the thickness decrease to monolayer, e.g., the black phosphorous. The dimensionality reduction from bulk to the monolayer limit does not increase the band gap evidently, since the individual monolayer is naturally well confined by the internal potential barriers, and the interlayer Van der Waals coupling is quite weak.

Based on the band structures obtained from the first-principles calculations above, we study the excitons in $(\text{PEA})_2\text{PbI}_4$ monolayer. The internal motion of exciton is governed by

$$\left[-\frac{\hbar^2}{2\mu} \nabla_{\rho}^2 + V_{2D}(\rho) \right] \psi = \mathcal{E} \psi. \quad (1)$$

where the reduced mass $\mu = m_e m_h / (m_e + m_h)$, the electron mass $m_e = 0.208m_0$, and the hole mass $m_h = 0.372m_0$. The electron mass and hole mass are adopted from the first-principles calculated band dispersions along Γ -L path in k -space, respectively. Considering the ultrathin thickness of the $(\text{PEA})_2\text{PbI}_4$ monolayer, the Keldysh potential²⁹ can be used to describe the Coulomb interaction between the electron and hole.

$$V_{2D}(\rho) = -\frac{e^2}{4\pi\epsilon_0\epsilon_2\rho_0} \frac{\pi}{2} \left[H_0\left(\frac{\rho}{\rho_0}\right) - Y_0\left(\frac{\rho}{\rho_0}\right) \right], \quad (2)$$

where $\rho = (\rho, \varphi)$ is the relative displacement between the electron and hole, the screening length of the PbI_4 layer $\rho_0 = r_0/\epsilon_2$, and $r_0 = \epsilon_1 L_w (1 + \epsilon_2/\epsilon_1^2)/2$. The relevant parameters in the Keldysh potential are defined as follows. For the sandwiched inorganic PbI_4 layer, the width $L_w = 6.36\text{\AA}$ ²³, and the relative permittivity $\epsilon_1 = 6.10$ ^{22,23}. For the organic barriers, the width $L_b = 9.82\text{\AA}$, and the relative permittivity $\epsilon_2 = 3.32$ ²³. The exciton binding energy \mathcal{E}_b can be obtained by applying the variational method to Eq.(1). With the parameters given above, the exciton binding energy is about $\mathcal{E}_b = 238.5$ meV, which agrees well with the experimental result 220-250meV^{23,30}. Correspondingly, the exciton spectrum of the $(\text{PEA})_2\text{PbI}_4$ monolayer (the red solid lines) is shown in Fig. 2(a). The exciton spectrum is calculated from Eq.(1).

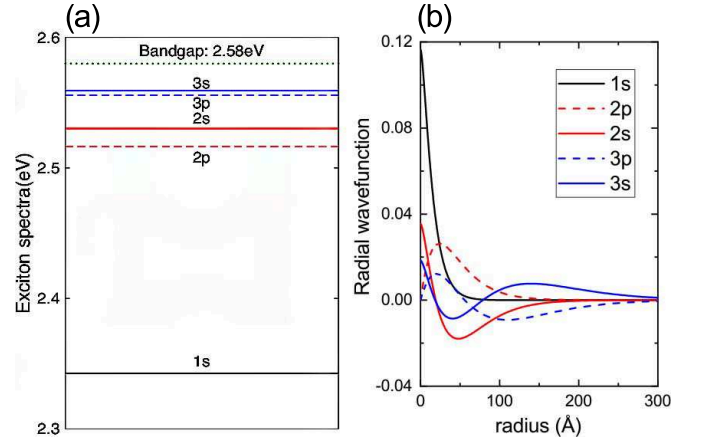


FIG. 2: (a) Exciton spectrum in perovskite monolayer estimated by the Keldysh model. The solid lines show the s states, while the dash lines show the p states. The dot green line gives the free carrier limit, which is determined by the band gap of the 2D perovskite. (b) The schematic of radial distribution of exciton wavefunctions.

The bandgap $E_g = 2.58\text{eV}$ as reported in Ref.²³, and the PL maximum $E_0 = E_g - \mathcal{E}_b \approx 2.34\text{eV}$, which is close to the experimental value 2.4eV²³ and 2.37eV²⁷.

When a perpendicular electric field is applied, the effective electron-hole interaction becomes dependent on the z -directional distribution of the electron (z_e) and hole (z_h). The Keldysh potential takes the form as

$$V(\rho, z_e, z_h) = -\frac{e^2}{4\pi\epsilon_0\rho} \int_0^\infty \frac{J_0(t)}{\epsilon_{mac}^{2D}(t/\rho, z_e, z_h)} dt, \quad (3)$$

where the dielectric function is expressed as

$$\epsilon_{mac}^{2D} \approx e^{q|z_e - z_h|} \left[\epsilon_2 + L_w q \frac{\epsilon_1}{2} \left(1 + \frac{\epsilon_2^2}{\epsilon_1^2} \right) \right]. \quad (4)$$

in the thin film limit. By expanding the equation of exciton motion Eq.(1) into three dimensional(3D) form, the exciton motions under the electric field are obtained,

$$\left[-\frac{\hbar^2}{2\mu} \nabla_{\rho}^2 - \frac{\hbar^2}{2M} \nabla_{\mathbf{R}}^2 + H_{e_z}(z_e) + H_{h_z}(z_h) + V(\rho, z_e, z_h) \right] \psi = \mathcal{E} \psi. \quad (5)$$

Here \mathbf{R} is the displacement of the center of mass (c.m.) of the exciton, $M = m_e + m_h$ is the c.m. mass of the exciton. $H_{e_z}(H_{h_z})$ denotes the single-particle Hamiltonian of the electron(hole) in the inorganic layer under the external electric field F . Variational exciton wavefunction³¹, associated with the l_e th electron and l_h th hole subbands,

$$\psi_{nm}^{l_e l_h}(\rho, z_e, z_h) = N^{l_e l_h} \zeta_{l_e}(z_e) \zeta_{l_h}(z_h) e^{-\sqrt{\left(\frac{z_e - z_h}{z_0}\right)^2 + \left(\frac{\rho}{a_0}\right)^2}} \quad (6)$$

is adopted for the 1s-type state in Eq.(5), with variational parameters a_0 and z_0 . The z -directional confinements of the electron and hole are included in ζ_{l_e} and ζ_{l_h} (See APPENDIX A).

For the 1s-type exciton state, the effects of perpendicular electric fields are limited. As shown in Fig 3(a), The band

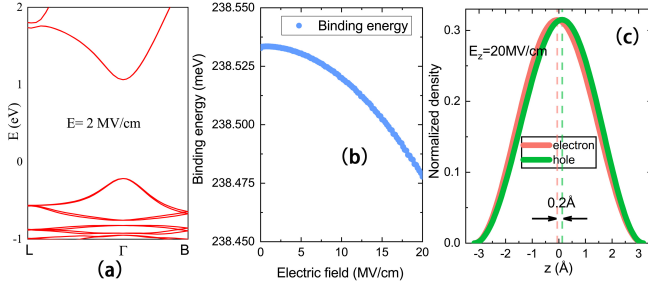


FIG. 3: (a) Band structures of (PEA)₂PbI₄ monolayers under external electric field of 2 MV/cm. (b) The exciton binding energies and strengths of perpendicular electric fields. (c) The electron-hole spatial separation as a function of perpendicular electric field. The effective separation is denoted by distance between centres of electrons (red lines) and holes (green lines).

gap of the perovskite monolayer remains unchanged under an electric field 2 MV/cm. Accordingly, the binding energy of the exciton varies slightly. From Fig 3(b), one can find the binding energy drops merely 0.06 meV as the strength of the perpendicular electric field increases up to a very strong electric field 20 MV/cm. The reason lies in the fact that, it is difficult to separate electrons and holes vertically, as shown in Fig 3(c), in presence of perpendicular electric field as strong as 20 MV/cm, the effective spatial separation between centres of holes and electrons d along the z -axis is less than 1 Å. This feature arises from the very strong confining potential (about 8eV) and weak inter-layer coupling.

Although perpendicular electric field changes extremely slightly the binding energies and Bohr radius of the perovskite monolayer, but it is efficient to align dipoles, change the exciton-exciton interactions utterly, and play a crucial role in the exciton BEC under the critical temperature.

The critical temperature for the BEC transition in the flakes of (PEA)₂PbI₄ monolayer is estimated by

$$T_c = \frac{\pi \hbar^2 n}{M k_B \ln(nS/2)} \quad (7)$$

where S is the area of the flake, and n is the exciton density. For a square flake, with $S = (20\text{nm})^2$ and $n = 5 \times 10^{12} \text{cm}^{-2}$, we obtain $T_c \approx 106\text{K}$. Therefore, the exciton condensation can be achieved at the temperature under liquid nitrogen regime in (PEA)₂PbI₄ monolayer.

Usually, the Gross-Pitaevskii (GP) equation is widely used to describe the condensate states. Considering laser pumping and exciton recombination process, the non-equilibrium exciton condensates in the perovskite monolayer with the lateral boundaries, can be described by complex Gross-Pitaevskii (cGP) equation within mean-field approach. Under a weak perpendicular electric field, the exciton-exciton interaction is dominated by repulsive dipole-dipole interaction (DDI), which can be expressed as V_{dd} in reciprocal space,

$$V_{dd}(\mathbf{Q}) = \frac{e^2 d^2}{\epsilon_0 \epsilon_1} \frac{2 \left[\left(1 + \frac{\epsilon_2}{\epsilon_1}\right) e^{x_Q} + \left(1 - \frac{\epsilon_2}{\epsilon_1}\right) e^{-x_Q} \right] - 4}{x_Q \left[\left(1 + \frac{\epsilon_2}{\epsilon_1}\right)^2 e^{x_Q} - \left(1 - \frac{\epsilon_2}{\epsilon_1}\right)^2 e^{-x_Q} \right]}, \quad (8)$$

with $x_Q = Qd$. Here d is the electron-hole separation introduced by the electric field. Thus the cGP equation is expressed as

$$i\hbar \partial_t \psi = \left[-\frac{\hbar^2}{2M} \nabla_{\mathbf{R}}^2 + V_c + H_{dd} + i\hbar (\hat{R} - \Gamma |\psi|^2) \right] \psi, \quad (9)$$

where \hat{R} is the pumping rate, $\Gamma = 1/2\tau_{ex}$ the recombination rate, and τ_{ex} the exciton lifetime. V_c denotes as the trap potential for excitons. It is worth noting that, convolution of $H_{dd} = V_{dd} * |\psi|^2$ stands for the DDI, which display a nonlinear behavior.

Considering the laser pumping is generally radial symmetric, while the perovskite flakes possess irregular shapes in practice, the disorders induced by the lateral boundary provide the scatterings to the optically generated excitons, and change the directions of their momentum. As a consequence, non-zero angular velocities appear at the edges of the flakes. In presence of the nonlinear DDI term of the flake boundaries, the exciton condensate state is sensitive to the local angular velocities raised by the lateral disorders, which behave as local potentials surrounding the condensate cloud. Therefore, the exciton vortices are expected to emerge in the perovskite monolayer flakes with constant laser pumping.

In order to demonstrate the vortex states, the complex GP equation(9) is solved by time-splitting spectral methods in combination with discrete sine transforms³²⁻³⁵. The pumping and decaying process in each time step is shown in APPENDIX B. The parameters for exciton vortex simulations in a square flake of (PEA)₂PbI₄ monolayer with length $L_0 = 400\text{nm}$, are listed as follows. The flake is sampled by a 512×512 mesh in real space, and the time step is set to be $5 \times 10^{-6} \text{ns}$, to reach high accuracy. The pump power is set to be $\hat{R} \approx 2 \times 10^{-3} \text{meV}$, and the exciton lifetime is $\tau_{ex} = 2\text{ns}$. A shallow harmonic potential is also introduced to mimic interface potential fluctuations in the quantum well structures, i.e., we set $V_c = V_0 R^2 / 2L_0^2$ for $R < L_0$ and $V_c = \infty$ for $R \geq L_0$, with $V_0 \sim 10\text{meV}$ and $R = |\mathbf{R}|$.

The simulated exciton vortices are shown in Fig. 4. The vortex is characterized by a rotation of the phase of the condensates wavefunction around the singular point by an integer multiple of 2π . As shown in Figure 4(a), the first occasional vortices emerge during the dynamic evolution of the exciton condensates at $T = 2.2 \text{ns}$. The eight vortices locate at the dark spots in the contour plot of the density of the exciton condensates wavefunction. The corresponding phase distributions in Fig. 4(b), indicate 2π phase shift around the singular points of the wavefunction, which indicate the existence of exciton vortices. As time goes by, the vortex patterns tend to reach dynamic equilibrium since $T = 5.8 \text{ns}$. From Fig. 4(c) and Fig. 4(d), one can find there are three vortices in the central area of the perovskite monolayer flake. The three vortices are stable and rotating persistently, as illustrated at $T = 8.5 \text{ns}$, and even $T = 25.1 \text{ns}$, respectively, as shown in Fig. 4(e) and Fig. 4(f). Since the evolution time of vortices patterns is comparable to the exciton lifetime, it is promising to observe exciton vortex patterns in (PEA)₂PbI₄ monolayers experimentally.

In summary, we study the exciton BEC and its vortices in

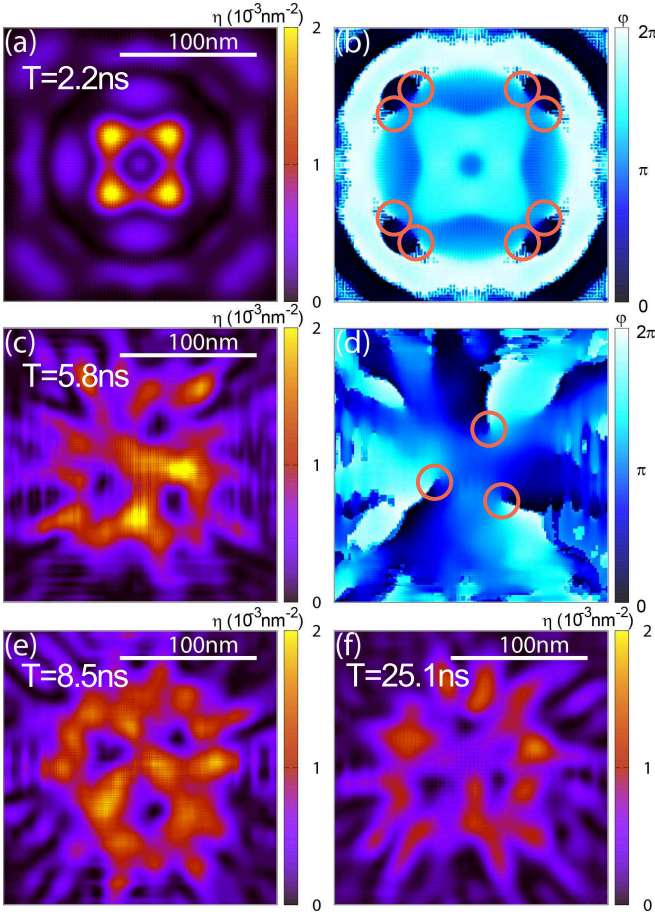


FIG. 4: Dynamic evolution of exciton vortices patterns in perovskite monolayer flake. (a) Contour map of the density of the exciton condensates wavefunction, at the first occurrence of occasional exciton vortices pattern. (b) The phase distributions of the exciton condensates wavefunction. (c) and (d), Density and phase distributions of exciton condensates wavefunction of the stable vortices pattern. (e) and (f), Density of exciton condensates wavefunction of the stable vortices pattern at $T = 8.5$ ns and $T = 25.1$ ns, respectively. The density $\eta = |\psi|^2$ is in the unit of 10^{-3}nm^{-2} . The orange circles show the locations of the vortices.

(PEA)₂PbI₄ monolayer, and calculated exciton binding energy 238.5 meV is in good agreement with experimental results. We find the perpendicular electric fields change slightly the binding energy and Bohr radius in (PEA)₂PbI₄ monolayer, but are efficient to align the electron-hole dipoles. With laser pumping, the repulsive dipole-dipole interaction created by the perpendicular electric field can drive the laterally confined excitons into various vortex patterns. The evolution time of those vortices is comparable to the exciton lifetime, and reach a stable pattern with certain number of vortices rotating at the center. Since the large exciton binding energy ensures the critical temperature of the exciton BEC within the liquid nitrogen regime, it is possible to realize stable exciton vortices in two-dimensional hybrid perovskite monolayers.

This work was supported by National Key R&D Programmes of China, Grant No. 2017YFA0303400,

2016YFE0110000. National Natural Science Foundation of China, Grant No. 11574303, 11504366. Youth Innovation Promotion Association of Chinese Academy of Sciences, Grant No. 2018148, and the Strategic Priority Research Program of Chinese Academy of Sciences, Grant No. XDB28000000.

Appendix A: Solution of the quantum confined exciton under electric field

The single particle $H_{e_z}(H_{h_z})$ denotes the Hamiltonian of the electron(hole) in the inorganic layer under the electric field F , i.e.,

$$\begin{cases} H_{e_z}(z_e) = -\frac{\hbar^2}{2m_e} \frac{\partial^2}{\partial z_e^2} + V_{\text{conf}}(z_e) + eFz_e \\ H_{h_z}(z_h) = -\frac{\hbar^2}{2m_h} \frac{\partial^2}{\partial z_h^2} + V_{\text{conf}}(z_h) - eFz_h \end{cases}, \quad (\text{A1})$$

where V_{conf} is the infinite-potential-barrier for the electron and the hole, since they are confined in the single inorganic layer. Eigenstates of Eq.(A1) are represented by the Airy functions Ai and Bi ,

$$\zeta_{l_e(l_h)}(z) = a_{l_e(l_h)} \text{Ai}(Z_{l_e(l_h)}(z)) + b_{l_e(l_h)} \text{Bi}(Z_{l_e(l_h)}(z)), \quad (\text{A2})$$

where $l_e(l_h) = 1, 2, \dots$ is the subband index of the electron(hole), and

$$\begin{cases} Z_{l_e} = -[2m_e / (e\hbar F)^2]^{1/3} (E_{l_e}^{(e)} - eFz) \\ Z_{l_h} = -[2m_h / (e\hbar F)^2]^{1/3} (E_{l_h}^{(h)} + eFz) \end{cases}. \quad (\text{A3})$$

Here $E_{l_e}^{(e)}(E_{l_h}^{(h)})$ is the l_e -th electron (l_h -th hole) subband energy. The parameters are normalized as

$$\begin{cases} a_l = [1 + \text{Ai}^2(Z_{l\pm}) / \text{Bi}^2(Z_{l\pm})]^{-1/2} \\ b_l = -a_l \text{Ai}(Z_{l\pm}) / \text{Bi}(Z_{l\pm}) \end{cases}$$

, with $Z_{l\pm} = Z_l(z = \pm L_w/2)$. The eigenenergies E_l are determined by the $(l-1)$ -zeros of

$$S(E_l) = \text{Ai}(Z_{l+}) \text{Bi}(Z_{l-}) - \text{Bi}(Z_{l+}) \text{Ai}(Z_{l-}). \quad (\text{A4})$$

Appendix B: Treatment of the pumping and decaying term

Here we deal with the time step containing the pumping and decaying term $i\partial_t\psi = i(\hat{R} - \Gamma|\psi|^2)\psi$, which can be written as

$$\partial_t\psi = (\hat{R} - \Gamma|\psi|^2)\psi. \quad (\text{B1})$$

Since the Eq.(B1) is real, we have

$$\partial_t\rho = 2(\hat{R} - \Gamma\rho)\rho. \quad (\text{B2})$$

Next we solve $\rho(t)$ from Eq.(B2), and obtain

$$\rho(t) = \frac{\hat{R}}{\Gamma} \frac{1}{1 + C e^{-2\hat{R}t}}, \quad (\text{B3})$$

with

$$C = \frac{\hat{R}}{\Gamma \rho_0} - 1.$$

Recalling Eq.(B1),

$$\psi'_1 = e^{\int_0^{\Delta t} (\hat{R} - \Gamma \rho(s)) ds} \psi_{1, \rho}(0) = \psi_1^2. \quad (\text{B4})$$

Putting Eq.(B3) into the integral in Eq.(B4), we have

$$\int_0^{\Delta t} (\hat{R} - \Gamma \rho(s)) ds = \hat{R} \Delta t + \frac{1}{2} \ln \left(\frac{\hat{R}}{\hat{R} + \Gamma \rho_0 (e^{2\hat{R}\Delta t} - 1)} \right) \quad (\text{B5})$$

The second-order time splitting can be written as

$$\psi(t + \Delta t) = e^{-i\frac{T}{2}\Delta t} e^{-i\frac{V}{2}\Delta t} e^{\int_0^{\Delta t} (\hat{R} - \Gamma \rho(s)) ds} e^{-i\frac{V}{2}\Delta t} e^{-i\frac{T}{2}\Delta t} \psi(t). \quad (\text{B6})$$

-
- * Electronic address: zhangdong@semi.ac.cn
† Electronic address: kchang@semi.ac.cn
- ¹ D. W. Snoke, J. P. Wolfe, and A. Mysyrowicz, *Phys. Rev. Lett.* **64**, 2543 (1990).
 - ² L. V. Butov, C. W. Lai, A. L. Ivanov, A. C. Gossard, and D. S. Chemla, *Nature* **417**, 47 (2002).
 - ³ L. V. Butov, A. Zrenner, G. Abstreiter, G. Bohm, and G. Weimann, *Phys. Rev. Lett.* **73**, 304 (1994).
 - ⁴ G. W. Rayfield and F. Reif, *Phys. Rev.* **136**, A1194 (1964).
 - ⁵ E. J. Yarmchuk, M. J. V. Gordon, and R. E. Packard, *Phys. Rev. Lett.* **43**, 214 (1979).
 - ⁶ J. Keeling and N. G. Berloff, *Phys. Rev. Lett.* **100**, 250401 (2008).
 - ⁷ K. G. Lagoudakis, T. Ostatnický, A. V. Kavokin, Y. G. Rubo, R. André, and B. Deveaud-Plédran, *Science* **326**, 974 (2009).
 - ⁸ I. Roy, S. Dutta, A. N. Roy Choudhury, S. Basistha, I. Maccari, S. Mandal, J. Jesudasan, V. Bagwe, C. Castellani, L. Benfatto, and P. Raychaudhuri, *Phys. Rev. Lett.* **122**, 047001 (2019).
 - ⁹ Y. D. Chen, Y. W. Huang, W. K. Lou, Y. Y. Cai, and K. Chang, *Phys. Rev. B* **00**, LP16278B (in press).
 - ¹⁰ A. Kojima, K. Teshima, Y. Shirai, and T. Miyasaka, *J. Am. Chem. Soc.* **131**, 6050 (2009).
 - ¹¹ J. You, L. Dou, K. Yoshimura, T. Kato, K. Ohya, T. Moriarty, K. Emery, C.-C. Chen, J. Gao, G. Li, and Y. Yang, *Nat. Commun.* **4**, 1446 (2013).
 - ¹² H. Zhou, Q. Chen, G. Li, S. Luo, T.-b. Song, H.-S. Duan, Z. Hong, J. You, Y. Liu, and Y. Yang, *Science* **345**, 542 (2014).
 - ¹³ W.-Y. Zhao, Z.-L. Ku, L.-P. Lv, X. Lin, Y. Peng, Z.-M. Jin, G.-H. Ma, and J.-Q. Yao, *Chin. Phys. Lett.* **36**, 028401 (2019).
 - ¹⁴ A. K. Jena, A. Kulkarni, and T. Miyasaka, *Chem. Rev.* **119**, 3036 (2019).
 - ¹⁵ P. K. Nayak, S. Mahesh, H. J. Snaith, and D. Cahen, *Nat. Rev. Mater.* **4**, 269 (2019).
 - ¹⁶ E. M. Tennyson, T. A. S. Doherty, and S. D. Stranks, *Nat. Rev. Mater.* **4**, 573 (2019).
 - ¹⁷ W.-R. Xie, B. Liu, T. Tao, G.-G. Zhang, B.-H. Zhang, Z.-L. Xie, P. Chen, D.-J. Chen, and R. Zhang, *Chin. Phys. Lett.* **34**, 068103 (2017).
 - ¹⁸ G. Grancini and M. K. Nazeeruddin, *Nat. Rev. Mater.* **4**, 4 (2019).
 - ¹⁹ L. N. Quan, M. Yuan, R. Comin, O. Voznyy, E. M. Beauregard, S. Hoogland, A. Buin, A. R. Kirmani, K. Zhao, A. Amassian, D. H. Kim, and E. H. Sargent, *J. Am. Chem. Soc.* **138**, 2649 (2016).
 - ²⁰ Z. Li, T. R. Klein, D. H. Kim, M. Yang, J. J. Berry, M. F. A. M. van Hest, and K. Zhu, *Nat. Rev. Mater.* **3**, 18017 (2018).
 - ²¹ M. M. Lee, J. Teuscher, T. Miyasaka, T. N. Murakami, and H. J. Snaith, *Science* **338**, 643 (2012).
 - ²² T. Ishihara, J. Takahashi, and T. Goto, *Phys. Rev. B* **42**, 11099 (1990).
 - ²³ X. Hong, T. Ishihara, and A. V. Nurmikko, *Phys. Rev. B* **45**, 6961 (1992).
 - ²⁴ O. Yaffe, A. Chernikov, Z. M. Norman, Y. Zhong, A. Velauthapillai, A. van der Zande, J. S. Owen, and T. F. Heinz, *Phys. Rev. B* **92**, 045414 (2015).
 - ²⁵ H.-H. Fang, J. Yang, S. Adjokatse, E. Tekelenburg, M. E. Kaminga, H. Duim, J. Ye, G. R. Blake, J. Even, and M. A. Loi, *Adv. Func. Mater.* **30**, 1907979 (2020).
 - ²⁶ M. D. Smith, B. A. Connor, and H. I. Karunadasa, *Chem. Rev.* **119**, 3104 (2019).
 - ²⁷ K.-z. Du, Q. Tu, X. Zhang, Q. Han, J. Liu, S. Zauscher, and D. B. Mitzi, *Inorg. Chem.* **56**, 9291 (2017).
 - ²⁸ T. T. H. Do, A. Granados del Águila, D. Zhang, J. Xing, S. Liu, M. A. Prosnikov, W. Gao, K. Chang, P. C. M. Christianen, and Q. Xiong, *Nano Lett.* **20**, 5141 (2020).
 - ²⁹ L. V. Keldysh, *Soviet Physics JETP* **29**, 658 (1979).
 - ³⁰ B. Cheng, T.-Y. Li, P. Maity, P.-C. Wei, D. Nordlund, K.-T. Ho, D.-H. Lien, C.-H. Lin, R.-Z. Liang, X. Miao, I. A. Ajia, J. Yin, D. Sokaras, A. Javey, I. S. Roqan, O. F. Mohammed, and J.-H. He, *Commun. Phys.* **1**, 80 (2018).
 - ³¹ D. A. B. Miller, D. S. Chemla, T. C. Damen, A. C. Gossard, W. Wiegmann, T. H. Wood, and C. A. Burrus, *Phys. Rev. B* **32**, 1043 (1985).
 - ³² W. Bao and Y. Cai, *SIAM J. Appl. Math.* **75**, 492 (2015).
 - ³³ W. Bao and Y. Cai, *Kinet. Relat. Mod.* **6**, 1 (2013).
 - ³⁴ W. Bao and Y. Cai, *Commun. Comput. Phys.* **24**, 899 (2018).
 - ³⁵ J. Sierra, A. Kasimov, P. Markowich, and R.-M. Weishäupl, *J. Nonlinear Sci.* **25**, 709 (2015).